AN ADAPTIVELY REFINED, FINITE-VOLUME MODEL OF WIND-INDUCED CURRENTS IN LAKE NEUSIEDL

Tamás KRÁMER and János JÓZSA

Budapest University of Technology and Economics
Department of Hydraulic and Water Resources Engineering
H-1111 Budapest, Műegyetem rkp 3, K mf. 4., Hungary
Phone: +36 1 463 1164
E-mail: kramer@vit.bme.hu

Abstract

Hydrodynamic processes greatly determine the morphological and ecological evolution of lakes such as Lake Neusiedl, which is extremely shallow and has an extended and patchy reed cover. The hydrodynamic response to prevailing wind events is explored by two-dimensional numerical modelling, including wind-current interaction and non-uniform wind shear stress distribution in the physical description. The high spatial variability of the processes justifies the use of an adaptive technique that adjusts the mesh resolution dynamically to the estimated solution error, without the intervention of the modeller. The solution algorithm incorporates a MUSCL-Hancock-type finite volume scheme on a quadtree-based Cartesian mesh. The model is used to predict representative steady-state circulations and the unsteady currents during a documented wind event. The simulated flow fields are compared to observations.

Keywords: wind, lake, shallow water equations, wave-current interaction, solution-adaptivity, quadtree mesh, MUSCL scheme, finite volume method.

1. Introduction

Lake Neusiedl is a shallow saline lake situated on the border of Hungary and Austria (*Fig. 5*), with a surface area of 310 km^2. The mean depth is 1.4 m in the pelagic zone and less than 0.5 m in the littoral areas covered by reed. Due to the mild slope of the lakebed, water level variations occasionally move the shoreline hundreds of metres during a single meteorological event. The lake has long been investigated from hydrological, hydrodynamic, morphological, water quality and hydrobiological points of view. Research activities focused on exploring the features in the existing conditions, moreover, on establishing measures in order to slow down unfavorable processes and improve the quality of water, sediment and aquatic vegetation. It is known that large-scale hydrological and shorter-scale hydrodynamic processes play a key role in all the other lake processes mentioned above. In the case of Lake Neusiedl, the magnitude of throughflow is far smaller than that of the wind-induced motion (except at the Hanság canal outlet, where local currents can be generated by high discharge).

The hydrodynamic response of the lake to prevailing wind events is explored here by two-dimensional (2D), depth-integrated modelling. The numerical solution to the shallow water equations is obtained using a high-resolution Godunov-type finite volume method on a Cartesian mesh. Formal second-order accuracy in space and time is provided by first-order reconstruction of the flow variables and a two-stage predictor-corrector time stepping. The high spatial variability of lake bathymetry and vegetation cover warrants the use of an adaptive technique that adjusts the mesh resolution dynamically to the estimated solution error. With adaptive mesh refinement and coarsening, the goal is to reallocate cells to those areas where they contribute more effectively to the overall solution accuracy. The adaptation is based on the *a posteriori* estimation of the solution error that is updated as the simulation proceeds. This adaptation procedure is automatic, with a number of global and local tuning parameters to accommodate steady and unsteady simulations. We use a quadtree-based hierarchical mesh that lends itself comfortably to local and dynamic refinement.

The 2D model outlined in this paper was applied to calculate wind-induced steady-state circulation in the whole Lake Neusiedl and to reproduce unsteady flow in one of its enclosed bays during an observed storm.

2. Depth-averaged Flow Modelling

In shallow lakes, horizontal water exchange and mixing, bed erosion and sediment transport are essentially driven by the wind. The bulk of these processes occurs during wind storms, as these are the relevant periods of momentum transfer to the lake. In such conditions, the turbulence induced by high wind and bed shear extends to the whole water column, hence the depth-averaged flow field is considered representative of the lakewide hydrodynamics. An approximate solution of the depth-averaged flow is obtained using a two-dimensional description in the horizontal plane.

The governing equations in two dimensions are the shallow water equations, which are derived by integrating the Reynolds-averaged Navier-Stokes equations along the vertical direction. They express the conservation of volume (*Eq.* 1) and momentum (*Eqs.* 2 and 3) for an incompressible fluid with a free surface. The shallow water equations in terms of the conservative variables are:

$$\frac{\partial h}{\partial t} + \frac{\partial p}{\partial x} + \frac{\partial q}{\partial y} = 0 \tag{1}$$

$$\frac{\partial p}{\partial t} + \frac{\partial}{\partial x}\left(\frac{p^2}{h}\right) + \frac{\partial}{\partial y}\left(\frac{pq}{h}\right) - \frac{\partial}{\partial x}\left(\frac{h}{\rho}T_{xx}\right) - \frac{\partial}{\partial y}\left(\frac{h}{\rho}T_{xy}\right) = \tag{2}$$
$$-gh\frac{\partial \zeta}{\partial x} + fq + \frac{\tau_{sx} - \tau_{bx}}{\rho}$$

$$\frac{\partial q}{\partial t} + \frac{\partial}{\partial x}\left(\frac{pq}{h}\right) + \frac{\partial}{\partial y}\left(\frac{q^2}{h}\right) - \frac{\partial}{\partial x}\left(\frac{h}{\rho}T_{yx}\right) - \frac{\partial}{\partial y}\left(\frac{h}{\rho}T_{yy}\right) = \qquad (3)$$

$$-gh\frac{\partial \zeta}{\partial y} - fp + \frac{\tau_{sy} - \tau_{by}}{\rho},$$

and

$$T_{xx} = 2\rho\nu_e\frac{\partial u}{\partial x}, \qquad T_{xy} = T_{yx} = \rho\nu_e\left(\frac{\partial u}{\partial y} + \frac{\partial v}{\partial x}\right), \qquad T_{yy} = 2\rho\nu_e\frac{\partial v}{\partial y},$$

where h = total flow depth; $\mathbf{q} : (p, q)$ = horizontal volume flux; t = time; g = acceleration due to gravity; T_{xx}, T_{xy}, T_{yx}, T_{yy} = elements of the depth-averaged effective turbulent stress tensor in vertical planes; ν_e = depth-averaged turbulent eddy viscosity; ζ = surface elevation; f = Coriolis parameter; $\tau_b : (\tau_{bx}, \tau_{by})$ = bed shear stress; $\tau_s : (\tau_{sx}, \tau_{sy})$ = surface shear stress; ρ = density of water; $\mathbf{v} : (u, v)$ = horizontal depth-averaged velocity.

The depth-averaged effective turbulent eddy viscosity is defined with the analytic, discretisation-dependent Smagorinsky model [16]:

$$\nu_e = C_S A\sqrt{\left(\frac{\partial u}{\partial x}\right)^2 + \left(\frac{\partial v}{\partial y}\right)^2 + \frac{1}{2}\left(\frac{\partial u}{\partial y} + \frac{\partial v}{\partial x}\right)^2},$$

where A = cell area; $C_S \approx 0.05$ for lakes.

The lake is set into motion by the wind drag on the water surface, therefore the representation of the wind shear stress distribution in the physical model is of key importance. The shear stress at the free surface is computed as

$$\tau_s = \rho_{\text{air}}C_{10}\mathbf{w}_{10}\left|\mathbf{w}_{10}\right|,$$

where ρ_{air} = density of air; C_{10} = wind drag coefficient; $\mathbf{w}_{10}$ = wind speed vector, adjusted to 10 m height above the water surface. The transition of the $\mathbf{w}(z)$ profile along the fetch due to changes in the surface roughness is taken into account by an internal boundary layer model, which yields a non-uniform, fetch-dependent shear distribution even in steady conditions [17].

2.1. *Wave-current Interaction in the Bottom Shear Stress*

Shallow waters are called so for the fact that the action of surface waves reaches the bed level. The combined wave-current boundary layer model is calculated by the method of Grant and Madsen [9], whose physical model assumes that near-bottom flow is influenced by the relatively low-frequency currents and high-frequency surface waves. In particular, the bottom boundary layer is assumed to consist of a small-scale oscillatory wave boundary layer (WBL) nested within a steadier current boundary layer. When the bottom velocity fluctuations due to the wave orbital

velocity are of the same order as the mean current velocties, the turbulence caused by waves enhances the momentum exchange near the boundary and causes the boundary shear stress to be much greater than that associated with the mean currents alone. Instead of simply adding the shear from current and waves, Grant and Madsen provide a nonlinear description of the wave-current interaction which is anisotropic because the unsteadiness only exists in the direction of the waves. They assume that a time-invariant eddy viscosity characterises the whole wave period and a logarithmic vertical velocity profile holds above the bottom boundary layer. Considering the angle between the current and waves ϕ_{wc}, the maximum total shear stress τ_m during a wave period is found as

$$\tau_m = \sqrt{\tau_c^2 + 2\left|\cos\phi_{wc}\right|\tau_c\tau_{wm} + \tau_{wm}^2},\tag{4}$$

where τ_c = current shear stress and τ_{wm} = maximum wave shear stress. It is the current shear stress that affects the momentum balance of the mean flow, i.e. $\tau_b = \tau_c$. The current shear stress is expressed in terms of the Darcy-Weisbach-type friction factor due to wave-current interaction f_{cw} as

$$\tau_c = \frac{1}{2}\rho f_{cw}\mathbf{v}\left|\mathbf{v}\right|.$$

The root-mean-square wave height (H_{rms}) and wave period (T_s) are predicted locally using the empirical-analytical approach of Sverdrup-Munk-Bretschneider for fetch-limited conditions. Based on these wave parameters, the wave action near the bottom boundary layer is estimated by linear Airy wave theory. Details of the wave model can be found in the Shore Protection Manual [19].

The semi-logarithmic plot in *Fig. 1* illustrates the effect of waves on the vertical velocity profile in the direction of the flow. Without the action of waves, the velocity profile is logarithmic (dashed line $u_c(z)$ in the figure). On the other hand, the velocity profile is piecewise logarithmic in the presence of a wave boundary layer (solid line $u_{cw}(z)$). Both profiles are reconstructed from the depth-averaged velocity of the 2D flow solution, $\bar{u}$. To be consistent with the depth-averaged origin of the velocity, the profile must pass through the point $(h/e, \bar{u})$. The velocity becomes zero at a height z_0 above the bottom. Depending on whether the flow is rough or smooth turbulent (as defined by Grant & Madsen), the bed roughness height z_0 is related to the Nikuradze roughness k_n as $z_0 = k_n/30$, or to the maximum wave shear stress as $z_0 = \nu/(9\sqrt{\tau_{wm}/\rho})$, respectively, ν = kinematic viscosity of water. The profile inside the wave boundary layer ($z < \delta_{cw}$) is a function of the total shear stress τ_m, whereas the profile above the WBL develops according to the shear induced by the mean current τ_c. As a consequence, the wave shear increases the velocity gradient above the WBL, hence τ_c will be higher with wave-current interaction than without. The increase in the shear stress can be translated into an increased, "apparent" bed roughness $z_{0a} > z_0$.

Although the maximum total shear stress does not directly enter the shallow water equations, τ_c and τ_{wm} are interconnected, therefore the calculation must
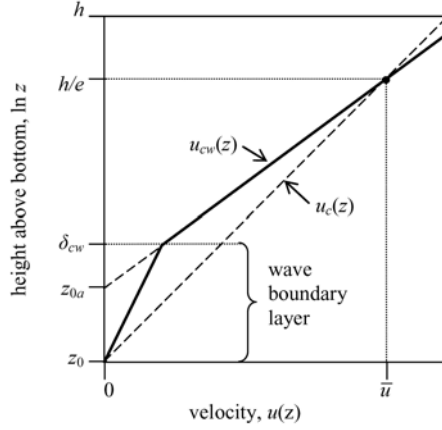
Fig. 1. Period-averaged velocity profile in the presence of waves $u_{cw}(z)$ and without waves $u_c(z)$. The vertical axis shows the height above bottom in logarithmic scale.

proceed iteratively by finding f_{cw} corresponding to the converged solution of τ_m. Initially, it is assumed that only the action of waves defines the shear stress, i.e. $\tau_m = \tau_{wm}$, $\tau_c = 0$. At the beginning of the iteration step, z_0 and f_{cw} are determined according to the turbulence regime and the ratio τ_c/τ_{wm}. Then the velocity profile in *Fig. 1* is reconstructed, which yields a new estimate of τ_c. To close this iteration step, τ_{wm} and τ_m are updated according to *Eq. 4*. The iteration continues until the change in τ_m in the current iteration step is less than the tolerance level set by the modeller. To speed up the calculation, the friction factor f_{cw} resulting from the wave-current interaction is updated less frequently than the flow solution (e.g. every 10th time step), and values of f_{cw} in intermediate time steps are approximated by linear interpolation. This approach, while greatly reducing simulation times, proved to be sufficiently robust, so that a more sophisticated updating scheme (such as one adapted to the acceleration of the flow) was not necessary.

If no interaction between the waves and currents is to be considered, the bed shear stress is simply calculated as

$$\tau_b = \frac{1}{2}\rho f_c \mathbf{v} \, |\mathbf{v}| \, .$$

For convenience, the bed roughness k_n is specified through Manning's empirical formula

$$k_n = \frac{30h}{e^{1+\kappa\sqrt{2/f_c}}}, \qquad f_c = 2\frac{gn^2}{h^{1/3}},$$

in which κ = von Kármán constant ($\sim$0.4); f_c = current friction factor; n = Manning's roughness coefficient.

2.2. Resistance due to Vegetation

In the vegetated littoral zones, reed stems and leaves increase flow resistance by causing velocity shear, hence turbulence, along the water column in addition to the bed shear. Describing the resistance due to vegetation using physical parameters related to the flow and the vegetation is an active area of research and a great number of approaches have been developed. Most of these approaches are specialised for either submerged, emergent or floating vegetation and none of them has yet gained such a wide acceptance for lacustrine conditions as Manning's formula for bed resistance. Among the reasons for this is the disparity of aquatic vegetation types and the difficulty of model parameterisation and calibration. In effect, costly remote sensing, image analysis techniques and field surveys are employed to demarcate vegetation patches with uniform physical properties. Furthermore, calibration requires information on currents or water surface gradients which is difficult to collect in dense vegetation and the upscaling of local measurements to the spatial resolution of the model is laden with uncertainty.

Flow resistance due to vegetation is modelled in this work by increasing Mannings's n locally according to vegetation type and density. In fact, the depth distribution in the reed covered zones of Lake Neusiedl is rather uniform. Therefore we expect that a depth-dependent vegetation drag model would not qualitatively improve the overall flow solution.

3. Quadtree-based Adaptive Mesh Refinement

Successful adaptivity strategies allocate computational effort where it reduces the error in the numerical solution most effectively. If the emphasis is on accurate and detailed results in a small area, the error is measured locally, perhaps as a pointwise deviation from the exact solution. If good overall accuracy is instead targeted, the error is interpreted as an integral of the deviation over the whole lake.

Two strategies are commonly used to extend structured grids with solution-adaptive capability: AMR and hierarchical mesh methods. AMR (Adaptive Mesh Refinement) methods cover the domain with dynamically changing, non-overlapping grid patches of uniform but different cell density [10]. A trade-off must be considered between the number of patches and the cost of transferring boundary values between the grids at every timestep. The major advantage of the AMR method is that each grid patch remains structured, which facilitates the application of parallel numerical algorithms.

On the other hand, the data structure of a hierarchical mesh is represented by linked quadtree. This allows more flexible modification of the mesh topology. Hierarchical meshes, as their name suggests, are composed of cells with different levels of refinement, set according to the desired local level of detail and solution accuracy (see e.g. [2, 6]). Refinement is isotropic and self-similar on a regular quadtree, since the cell aspect ratio is kept constant and the subdivision to half of the

original size can be repeated recursively for any cell in the mesh. The encapsulation of cells with different level of subdivision forms a system of hierarchy which can be represented by a directed tree. When a cell is refined, it becomes a *parent*, and four new branches are created for each *child* cell. A parent cell can also be coarsened by aggregating its children and pruning their branches. The actual mesh is composed of the *leaf* cells, i.e. those cells at the bottom of the hierarchy which have no children.

The advantage of hierarchical meshes compared to unstructured ones is that the initial mesh generation is fast, straightforward and automatic. Local adaptation has only a local effect on the mesh, therefore the algorithms of refinement and especially coarsening are simpler and faster, as no global remeshing is needed. Furthermore, cells are not distorted during adaptation. Cell size variability can be controlled, namely by smoothing out abrupt differences in the refinement level, though at the expense of redundant subdivisions. On the other hand, a disadvantage of hierarchical Cartesian meshes is that without special techniques, they are difficult to adapt to anisotropy and non-Cartesian boundaries. Hierarchical mesh methods have long been used in aerodynamics (e.g. [4, 6]), and they also emerge as the basis of shallow flow models. Early work in this direction includes the quadtree-based finite difference model of GÁSPÁR et al. [8]. More recently, BORTHWICK et al. [2] solved the shallow water equations using a staggered upwind finite volume scheme, while ROGERS et al. [14] presented a Godunov-type scheme for this purpose.

The mesh generator initially refines the mesh to the manually prescribed cell sizes. Minimum target and maximum cell size can be assigned to zones as well as to internal and external boundaries, in order to represent faithfully the varied bathymetry, vegetation patches and generally oriented shorelines in the model. The mesh is then dynamically adapted as the simulation proceeds, based on solution error estimators that guide the allocation and reallocation of new cells. Numerous error indicators have been developed that allow the estimation of the error without knowing the exact solution. The error estimator chosen for solution-adaptation in the present model is based on the reconstruction error of the velocity (τ_a), weighted by the cell area. In cell i, the error is estimated as

$$\tau_{a,i} = \frac{A_i}{n_j} \sum_j \left| \mathbf{v}_j - \left[\mathbf{v}_i + \nabla \mathbf{v}_i \cdot \left(\mathbf{r}_j - \mathbf{r}_i \right) \right] \right|,$$

where $j \in$ neighbours of cell i; n_j = number of neighbours. Hence, the error is derived from the average deviation between $\mathbf{v}$ in neighbouring cells j and $\mathbf{v}$ reconstructed is those cells by linear extrapolation from cell i. A nondimensional adaptation indicator is then derived from the error estimator for each leaf and parent cell i:

$$a_i = \frac{\tau_{a,i}}{P_{1-s_a}(\tau_a)},$$

where P_q = the q-quantile of τ_a; s_a = sensitivity of the adaptation to the error estimator. Standardising the error estimator using this quantile is a robust and general method that accommodates outliers and makes no assumption on how τ

is distributed. To reduce the occurrence of alternating refinement and coarsening in subsequent adaptations, the quantile is taken not only for leaf cells, but also for their parents.

The adaptation procedure follows by flagging all leaf cells for refinement for which $a_i > 1$. Next, parent cells are coarsened if $a_i < a_{coa}$ holds for the parent, where a_{coa} is a coarsening threshold parameter. We imposed further restrictions to coarsening: the children of the coarsened parent must be leaves created during a previous adaptive refinement, and none of them should be flagged for refinement in the actual step. Finally, refinement is carried out for leaf cells already flagged. In this last step, the total number of cells in the mesh is limited by prioritising the refinement with respect to a_i. Namely, if the total cell count is exceeded with all the requested refinement, only cells with the highest a_i value are actually refined. For convenience, the limit to the total cell count (n_{max}) is given as a multiple of the cell count in the initial mesh. Any refinement may trigger the refinement of neighbours to ensure the smooth variation of cell size. The modeler has control on the solution adaptation by tuning s_a, a_{coa} and n_{max}. A low sensitivity ($s_a < 0.1$) means that the threshold for τ_a is raised and fewer cells are flagged for refinement. On the other hand, setting s_a high > 0.25) makes it likely that the refinement will be limited by n_{max}.

The properties of new cells (bottom elevation, flags and zone type) are not derived from the existing mesh but re-rendered from the digital elevation model and the boundary polygons. This allows the model to discover, as a cell is being refined, small-scale land and coverage features that were smeared before due to insufficient resolution. The solution, on the other hand, is projected to the new mesh by linear interpolation based on the last **u** values. Since the bottom surface has also changed, the surface elevation must be adjusted afterwards so that volume is conserved during adaptation.

4. A Finite-volume Flow Solver

4.1. *High-resolution MUSCL Method*

The Cartesian quadtree-mesh lends itself conveniently to the definition of cell-centered control volumes. This is the reason why an unsplit, collocated Godunov-type finite-volume scheme was adopted in this work, whereby the flow state variables are located in the cell centre and represent the average flow state over the cell. To accommodate the flux-oriented framework of Godunov schemes, the integral form of the shallow water equations (*Eqs.* 1–3) is used:

$$\frac{\partial}{\partial t} \int_A \mathbf{u} \, dA + \int_A \left(\frac{\partial \mathbf{f}_1}{\partial x} + \frac{\partial \mathbf{g}_1}{\partial y} \right) dA = \int_A \left(\frac{\partial \mathbf{f}_2}{\partial x} + \frac{\partial \mathbf{g}_2}{\partial y} \right) dA + \int_A \mathbf{s} \, dA \quad (5)$$

The flow state vector $\mathbf{u}$, the inviscid flux vectors $\mathbf{f}_1$, $\mathbf{g}_1$, the viscous flux vectors $\mathbf{f}_2$, $\mathbf{g}_2$ and the vector of the source terms $\mathbf{s}$ are defined as follows:

$$\mathbf{u} = \begin{bmatrix} \zeta \\ p \\ q \end{bmatrix}, \qquad \mathbf{f}_1 = \begin{bmatrix} p \\ \frac{p^2}{h} + \frac{g}{2}h^2 \\ \frac{pq}{h} \end{bmatrix}, \qquad \mathbf{g}_1 = \begin{bmatrix} q \\ \frac{pq}{h} \\ \frac{q^2}{h} + \frac{g}{2}h^2 \end{bmatrix},$$

$$\mathbf{f}_2 = \begin{bmatrix} 0 \\ \frac{h}{\rho}T_{xx} \\ \frac{h}{\rho}T_{xy} \end{bmatrix}, \qquad \mathbf{g}_2 = \begin{bmatrix} 0 \\ \frac{h}{\rho}T_{yx} \\ -\frac{h}{\rho}T_{yy} \end{bmatrix},$$

$$\mathbf{s} = \begin{bmatrix} 0 \\ -g\left(\frac{1}{2}\frac{\partial z_b^2}{\partial x} - \zeta\frac{\partial z_b}{\partial x}\right) + fq + \frac{\tau_{sx}-\tau_{bx}}{\rho} \\ -g\left(\frac{1}{2}\frac{\partial z_b^2}{\partial y} - \zeta\frac{\partial z_b}{\partial y}\right) - fp + \frac{\tau_{sy}-\tau_{by}}{\rho} \end{bmatrix},$$

in which z_b is the bottom elevation.

In the above expressions, we employ the source term balancing described in Reference [3] which ensures that no flow is initiated at steady state on uneven topography due to the different discretisation of the pressure and bed slope terms. The key of the balancing method is to substitute the identity $h \equiv \zeta - z_b$ in the term $-gh\nabla\zeta$, which is then split into a pressure and a bed slope source term in such a way that the balance is also satisfied in the discrete case. On a similar line, ROGERS et al. [14] reformulate the flux function instead of the source term. A comparison of the two splitting methods for wind-driven benchmark problems with uneven bathymetry showed no discernible difference in the results.

With the finite-volume method, the divergence theorem is used to evaluate surface integrals of the gradient in *Eq.* (5) as path integrals around the control volume:

$$A\frac{\partial u}{\partial t} + \sum_{\text{edges}}(\hat{\mathbf{f}}_1\Delta y + \hat{\mathbf{g}}_1\Delta x) = \sum_{\text{edges}}(\mathbf{f}_2\Delta y + \mathbf{g}_2\Delta x) + \mathbf{s},$$

where the summation is made for all edges of the control volume. From the perspective of the finite volume solver, the quadtree mesh appears as a general unstructured one, where cells have an arbitrary number of edges. A cell side with one or more hanging nodes is consequently treated as multiple independent edges.

According to Godunov-type methods, $\hat{\mathbf{f}}_1$ and $\hat{\mathbf{g}}_1$ are the numerical fluxes arising from a local Riemann problem at each cell edge. The Riemann problem is an initial value problem, where the time update of the cell-averaged flow states is determined based on the initially discontinuous, piecewise constant profile of the flow state on both sides of the edge. Several approximate Riemann solvers were proposed for the shallow water equations that simplify and speed up significantly the solution of the Riemann problem. In this work, the HLLC Riemann solver is adopted [7], because it was found to be as robust for problems involving wetting

and drying as its simpler variant, the HLL Riemann solver, but is more accurate in describing transverse wave propagation in multidimensional problems.

Godunov's scheme is only first-order accurate in space, which is known to cause significant numerical diffusion in the presence of sharp velocity gradients. The extension of the method to second-order spatial and temporal accuracy is achieved by the MUSCL-Hancock method, namely through a piecewise linear reconstruction of the flow variables and an explicit, non-conservative predictor and a conservative corrector time-stepping scheme. Linear reconstruction requires the approximation of the gradient of $\mathbf{u}$ in each cell. Since a general quadtree mesh gives rise to diverse neighbour topologies, the gradient is calculated generally, based on neighbouring cell-averaged values. For that purpose, a closed path connecting neighbouring cell centres is determined around the cell of interest and the gradient is expressed numerically using the divergence theorem:

$$\nabla \mathbf{u} \approx \frac{1}{2A_{\text{path}}} \sum_{\text{edges}} \ell(\mathbf{u}_p + \mathbf{u}_n)\mathbf{n},$$

$$2A_{\text{path}} = \sum_{\text{edges}} (x_n - x_p)(y_n + y_p),$$

where A_{path} = area enclosed by the path; ℓ, $\mathbf{n}$ = length and unit normal of an edge, respectively. The summation is undertaken for all edges of the path, and subscripts n and p refer to the starting and ending cell indices of an edge, respectively. The particular order in which the path connects the cell centres does not matter, but the same vertex order must be kept for A_{path} as for $\nabla \mathbf{u}$. The choice of the cells making up the closed path is not unique: unlike in other path-integral gradient schemes [4, 6], the diagonal neighbours are included only if the adjacent side neighbours are dry or external cells (*Fig. 2*). This path selection method yields smaller stencils and reduces to central differences on regular grids. The differential operator of the diffusive fluxes is discretised according to the path-integral reconstruction method of COIRIER [4] with "diamond path and simple vertex weighting".

(a)   (b)
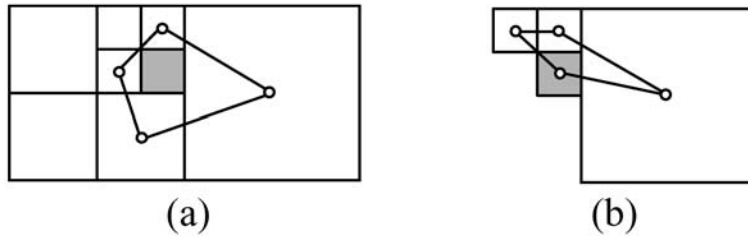
Fig. 2. Polygons for the Green-Gauss gradient calculation in a typical inner (a) and boundary (b) cell.

The equations in their integral form admit discontinuous solutions involving hydraulic jumps and bores. This "shock-capturing" attribute explains why the development of Godunov-type methods was mainly motivated by applications to transcritical flow problems. Yet, since wind-induced currents in shallow lakes are subcritical, the reason why we chose a Godunov method was that the control volume conveniently coincides with the rectangular quadtree cell for all three state variables.

In the predictor step of the MUSCL-Hancock scheme, the solution is updated from the current time level t^n to an intermediate time level $t^{n+1/2}$ without the use of any Riemann solver. The gradient is first determined, then the state variables are extrapolated to the edge midpoints as

$$\mathbf{u}_f^n = \mathbf{u}_i^n + \nabla \mathbf{u}_i^n \cdot (\mathbf{r}_f - \mathbf{r}_i),$$

with $\mathbf{u}_f$, $\mathbf{u}_i$ = flow state vector on the edge and in the cell centre, respectively; $\mathbf{r}_f$, $\mathbf{r}_i$ = position vector to edge and cell centroids, respectively. Two flow states are reconstructed for the common vertical edge in *Fig. 3*: the left state $\mathbf{u}_L$ is extrapolated from the state of the left neighbour $\mathbf{u}_i$, the right state $\mathbf{u}_R$ from $\mathbf{u}_j$ of the right neighbour. It should be noted that it is the surface elevation, which is directly reconstructed, whereas the flow depth entering the flux $\mathbf{f}_1$ and $\mathbf{f}_2$ is obtained at the edge as $h \equiv \zeta - z_b$. The bottom elevation at the edges is the average of the central values in the two adjacent cells.
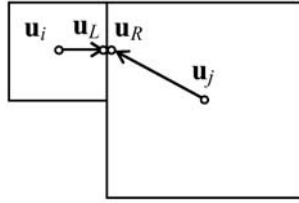
Fig. 3. Reconstruction of left and right flow states $\mathbf{u}_L$ and $\mathbf{u}_R$.

The solution update for the predictor step is

$$\mathbf{u}_i^{n+1/2} = \mathbf{u}_i^n - \frac{\Delta t}{2A_i} \left[\sum_{\text{edges}} (\mathbf{f}_1(\mathbf{u}_f^n)\Delta y + \mathbf{g}_1(\mathbf{u}_f^n)\Delta x) \right]$$
$$- \frac{\Delta t}{2A_i} \left[\sum_{\text{edges}} (\mathbf{f}_2(\mathbf{u}^n)\Delta y + \mathbf{g}_2(\mathbf{u}^n)\Delta x) \right] + \frac{\Delta t}{2}\mathbf{s}(\mathbf{u}_i^n).$$

This step is non-conservative, because a separate inviscid flux contributes to the left and right (or upper and lower) neighbour of an edge, based on the reconstructed flow state on the respective side as shown in *Fig. 4*.
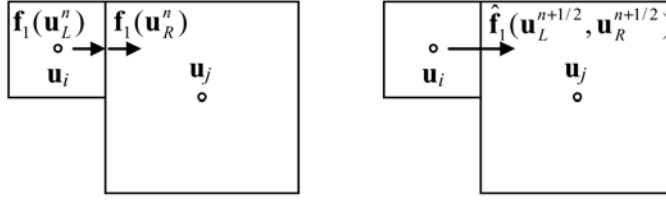
Fig. 4. Inviscid fluxes in the predictor (left) and corrector (right) step.

The corrector step uses this intermediate flow state to reconstruct the flow states at the edges with the gradients computed in the predictor step:

$$\mathbf{u}_f^{n+1/2} = \mathbf{u}_i^{n+1/2} + \nabla\mathbf{u}_i^n \cdot (\mathbf{r}_f - \mathbf{r}_i)$$

Then a unique numerical flux is evaluated on each edge using the HLLC Riemann solver using the left and right states separated by a discontinuity. Finally, the update of the corrector step is

$$\mathbf{u}_i^{n+1} = \mathbf{u}_i^n - \frac{\Delta t}{A_i}\left[\sum_{\text{edges}}(\hat{\mathbf{f}}_1(\mathbf{u}_L^{n+1/2}, \mathbf{u}_R^{n+1/2})\Delta y + \hat{\mathbf{g}}_1(\mathbf{u}_L^{n+1/2}, \mathbf{u}_R^{n+1/2})\Delta x)\right]$$

$$- \frac{\Delta t}{A_i}\left[\sum_{\text{edges}}(\mathbf{f}_2(\mathbf{u}^{n+1/2})\Delta y + \mathbf{g}_2(\mathbf{u}^{n+1/2})\Delta x)\right] + \Delta t\, \mathbf{s}(\mathbf{u}_i^{n+1/2})$$

The advantage of the MUSCL-Hancock scheme is that it yields second-order accuracy with half the number gradient calculations and Riemann solutions compared to a MUSCL scheme with second-order TVD Runge-Kutta time stepping [15], while also being overall conservative.

4.2. *Boundary Conditions*

A no-slip wall boundary condition is prescribed along the lake boundary via the reconstruction procedure. In cells near the boundary, the gradient of the flow state includes only the wet cells, as shown in *Fig. 2b*. The flow state on the inner side of a boundary edge is reconstructed as usual and **u** on the outer side is mirrored about the edge. No other measures must be taken and the flux calculation proceeds as for internal edges. This boundary procedure is simple to implement and mass-conservative. It has been found (e.g. in Reference [1]) that models based on Cartesian meshes suffer from a necessarily stepped discretization of boundaries that are not aligned with the mesh, especially in conservative finite-volume methods.

Redundant refinement along boundaries only slightly alleviates this problem, instead the problem calls for a resolution at a lower level, for example using so-called "cut-cells" [6] or the immersed boundary method [18].

Even during steady-state simulations, water may recede from some previously flooded areas or, oppositely, dry areas may become wet. In both cases, the momentum equations lose their mathematical validity where the flow depth approaches zero, because the terms involving the velocity grow beyond physical bounds. Therefore, the model must be equipped with a dynamic procedure to handle very shallow flow and laterally moving water boundaries. The wetting-and-drying technique presented by Zhao and his co-workers [20] is implemented in the framework of our finite-volume solver. The principle of the technique is to distinguish fully wet, partly wet and dry cells based on the water depth in the cell centre and on the edges. The momentum equation is then modified in partly wet and dry cells so as to avoid numerical instabilities while allowing the advance and recession of the wave front.

4.3. Local Time Stepping

The condition for stability of the explicit, unsplit MUSCL-Hancock scheme is based on the CFL (Courant-Friedrich-Lewy) number. The upper limit of the timestep is determined for each cell using

$$\Delta t_{i,\max} = \frac{\alpha_{CFL}}{s_{x,i}/\Delta x + s_{y,i}/\Delta y},$$ (6)

where α_{CFL} = maximum allowed CFL number; Δx, Δy = cell dimensions; $s_{x,i}$, $s_{y,i} = \max(|s_L|, |s_R|)$ is the maximum wavespeed over all edges of the cell in the respective direction, s_L, s_R = left and right-going wavespeeds obtained from the HLLC Riemann solver [7]. Employing a global timestep that is limited to the smallest allowable timestep in the mesh ($\Delta t_{\min}$) is rather restrictive, since the highly varied cell size in a typical quadtree mesh gives rise to an equally high inhomogeneity in the CFL number.

Instead of resorting to an implicit time integration scheme, a time-accurate local time stepping (LTS) is introduced to the explicit MUSCL-Hancock scheme. Cells are individually integrated in time, at a rate near the optimal CFL = 1. We adopt the synchronization technique proposed by KLEB et al. [12], which restricts the actual timesteps to be a power-of-two multiple of the global minimum timestep. A speedup factor of 1.5–2 can typically be reached, which is a significant, although not fundamental improvement over the global time stepping approach. CROSSLEY et al [5], who applied this LTS scheme to the de Saint-Venant equations, report that solution accuracy was not impaired.

5. Unsteady Flow in Fertőrákos Bay

The unsteady response of Lake Neusiedl to a typical measured storm was simulated, with special attention to the circulation in the Fertőrákos Bay. The Bay is prone to upsilting, as sediment-laden waters pushed by the prevailing north-northwesterly winds penetrate the southern part of the lake and drop much of the suspended load due to the sheltering of the vegetation. On the long term, interacting sediment accumulation and reed proliferation have created unfavourable conditions for boat traffic, recreation and aquatic fauna. The restoration measures which are being undertaken are supported by a detailed investigation of the exchange mechanisms in the Bay. During stormy weather, a person-assisted scanning of wind-induced currents can hardly be undertaken with a current meter attached to a moving vessel, yet these are the relevant periods of transport. Instead, the velocity field is typically sampled at discrete points over a longer time using fixed, autonomous current meters. We attempted to reproduce currents measured during a representative two-day period of a measurement campaign which focused on the Fertőrákos Bay. Six *Aanderaa RCM-7* type current meters were deployed in the Bay and recorded local horizontal currents at about mid-depth. The measurement technique is described by JÓZSA et al. [11].

The flow parameters of the steady-state simulation were set to the following: initial water level $\eta = 115.65$ m above sea level; maximum CFL number $\alpha_{CFL} = 0.8$; Smagorinsky coefficient $C_S = 0.05$; Coriolis coefficient $f = 10^{-4}$ s^{-1}. The surface shear stress was computed based on the wind measured above water at Station 2 (topmost stick plot in *Fig. 10*, at a height of 3 m; wind drag coefficient over water $C_{10} = (0.8 + 0.065\,|\mathbf{w}_{10}|) \cdot 10^{-3}$. The Manning coefficients were calibrated beforehand to a six-day storm (4/26–5/2/1992), when ten simultaneous measurements covering the whole lake were available. We minimized the time-integrated root-mean-square of the differences between simulated velocity vectors and those recorded by current meters. Minimization was driven by the inverse modelling tool UCODE [13], resulting in a Manning coefficient $n_{\text{lake}} = 0.028$ s/m$^{1/3}$ for the open lake and $n_{\text{reed}} = 0.18$ s/m$^{1/3}$ in reed covered areas. The roughness height of the reed used in the internal air boundary layer model was estimated as $z_{0,\text{reed}} = 0.2$ m, based on simultaneous data from two wind stations situated along a line directed to prevailing winds.

In order to increase the level of detail in Fertőrákos Bay, the initial cell size was set to 100–200 m there and to 400–800 m elsewhere in the lake, as shown in *Fig. 6*. Mesh generation was controlled by rendering 400 polygons consisting of more than 16,000 segments in total. The ragged reed boundary, digitized from a large scale map, was very detailed and accounted for the complexity of the polygons. It is clear that an efficient solution-adaptive model requires that the elementary operations of mesh modification be done quickly, especially that the coverage and bathymetry map is re-rendered after every adaptation step. With our mesh generator, the initial mesh was created in less than 1 s.

Bed elevation was determined at the cell centroids using a digital terrain
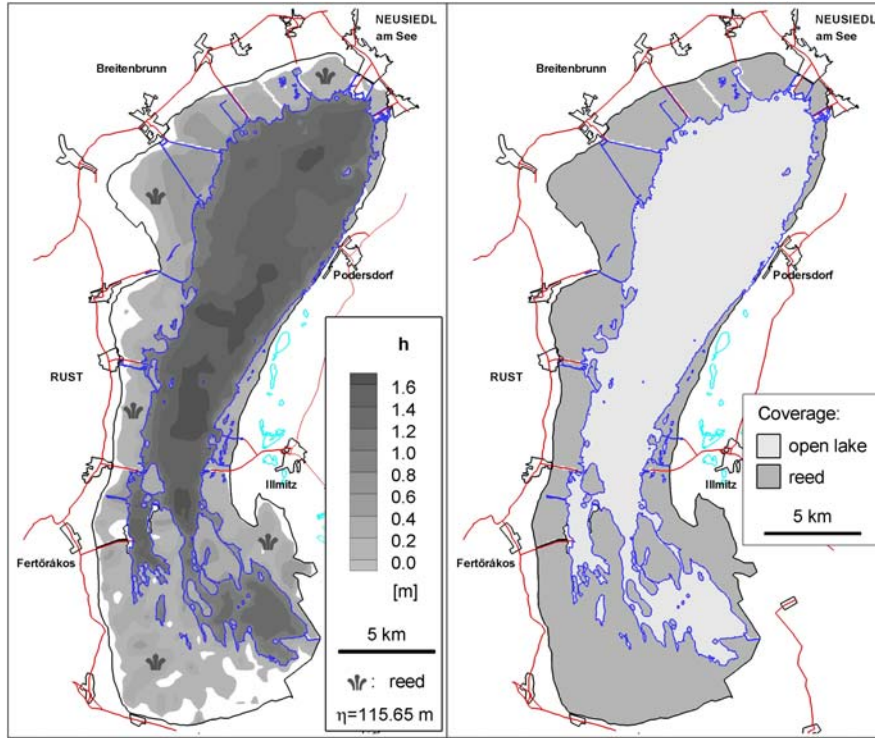
Fig. 5. Bathymetry and coverage map of Lake Neusiedl.

model (DTM) given on a regular grid, taking into account the resolution difference between the mesh and the DTM. The value of z_b was interpolated linearly in cells smaller than the DTM resolution, whereas in larger cells, it was obtained by area – weighted averaging of the underlying DTM nodes. This technique has several advantages: it yields the same storage volume as the original DTM, eliminates errors associated with pointwise sampling (known as aliasing in digital signal processing literature), and weakens disturbances inevitably introduced when the bathymetry is re-evaluated in refined cells.

The mesh was adapted to the solution hourly, with an adaptation sensitivity $s_a = 0.2$ and coarsening parameter $a_{coa} = 0.1$. Adaptation was confined to the Bay area, with a cell size limited to ≥ 50 m and a cell count limited to $\leq 3\times$ the initial count. No significant cell redistribution was observed after the initial refinement, so the right mesh in *Fig. 7* is actually characteristic to the whole simulation. The refinement indicator was apparently sensitive in the straits and interfacial regions. A snapshot of the number of local time stepping levels m (*Fig. 8*, left panel) indicates that the minimum timestep dictated by *Eq.* (6) has a highly uneven distribution. The local CFL number, defined as $2^{m_i}\,\Delta t_{\min}/\Delta t_{i,\max}$, is by construction

Fertőrákos Bay
magnified
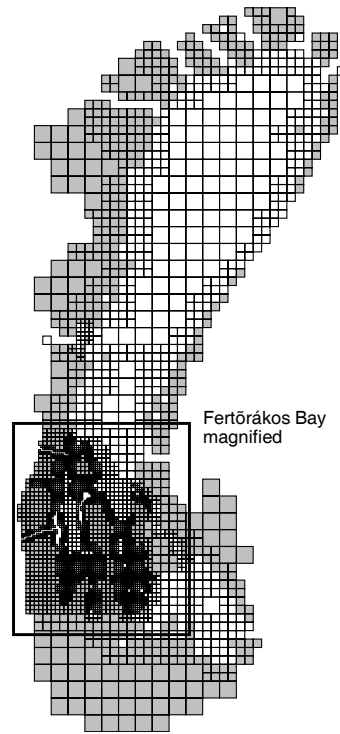
Fig. 6. Initial mesh generated for the lake, with refinement manually increased in the
        Fertőrákos Bay

higher than 0.5 α_{CFL} thanks to LTS, except where the level was reduced by smooth-
ing the distribution of *m* (*Fig. 8*). The average CFL number for the whole lake was
0.735 α_{CFL} during that timestep, while the $P_{0.1}$ and $P_{0.9}$ quantile was 0.501 α_{CFL}
and 0.939 α_{CFL}, respectively. Without LTS, the average CFL number would have
been as low as 0.443 α_{CFL}, what represents a 70% run-time increase.

The instantaneous velocity vector field resampled to a uniform pattern is
shown in *Fig. 9*. Due to their shallowness and roughness, reed covered zones
impose high hydraulic resistance to the flow and therefore constitute a barrier to the
water exchange. The currents measured at six stations are laid over the simulated
velocity field with 6× magnification. These measurements were collected at 0,5
m height above the bed surface with 10-minute integral averaging. Simulation and
pointwise measurements confirm that the uneven distribution of water depth and
surface shear stress gives rise to a clockwise gyre in the Fertőrákos Bay.

Comparing measured and simulated velocity time series is a challenging test
for any lake model. The amplitude and phase response of the lake to wind forcing is
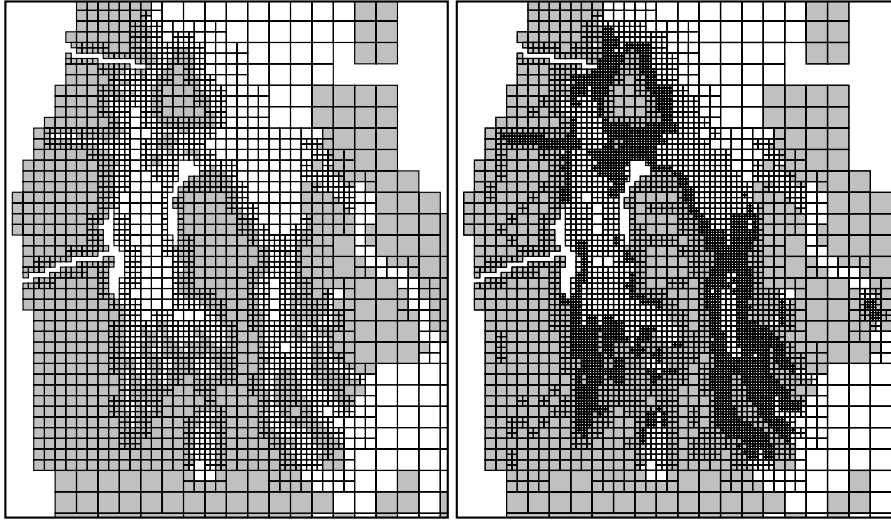
Fig. 7. Magnified view of the computational mesh in the Fertőrákos Bay. Left: at the beginning of the simulation. Right: after dynamic adaptation to the solution.

reproduced closely at Station 1 (*Fig. 10*). In constrast, there is a constant deviation from measurements at Station 4. One must consider however that these measurements correspond to horizontal velocities observed at a certain height, whereas the 2D model yields depth- and cell-averaged velocities, which generally differ in both amplitude and direction. Profiling current meters would allow a better insight into the actual vertical structure of the flow and a more direct comparison with the simulation results. Moreover, local mesh refinement around points of comparison can be imposed to decrease the horizontal averaging effect of the finite mesh resolution.

The power spectral density (PSD) function of the velocity gives a different insight into the performance of the model as it represents the frequency response of the lake. The PSD of the observed and simulated velocity at Station 4 shows (*Fig. 11*) that most of the spectrum, especially the peaks corresponding to different seiche modes, are reproduced reasonably well in the model. It is expected that one benefit of adaptive refinement is an improved representation of the bathymetry which is necessary for an accurate estimation of wave celerities. The difference observed in the stick plots (*Fig. 10*) is shown to be caused by the discrepancy in the lowest frequencies, which points to a poor approximation of the local circulation.
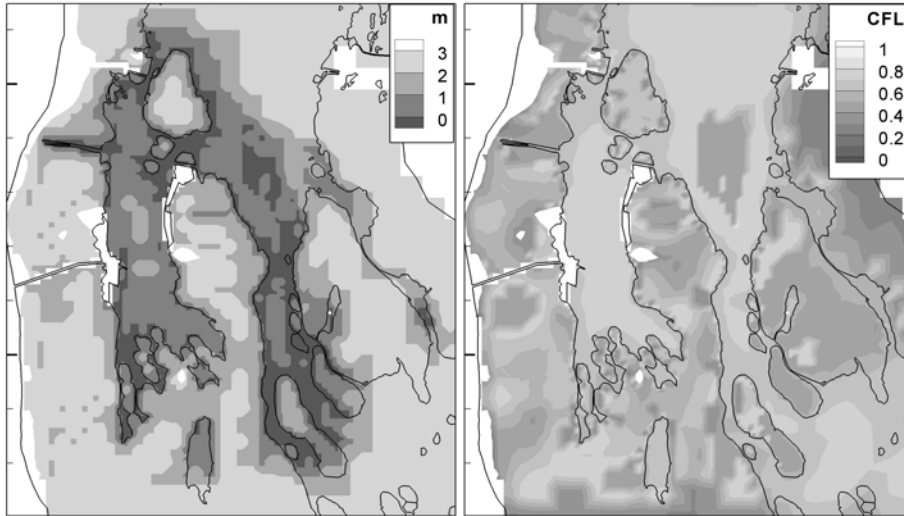
Fig. 8. Number of time subdivisions of the local time stepping scheme (left) and the CFL efficiency (right) in the Bay for the same instant as in *Fig. 9.*
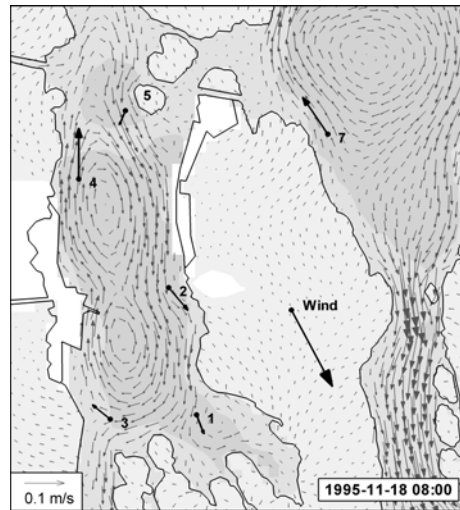
Fig. 9. Computed instantaneous velocity field in the Bay and six local velocities observed using current meters (shown with magnified black arrows). The simultaneous wind is also shown. Shading is according to depth.
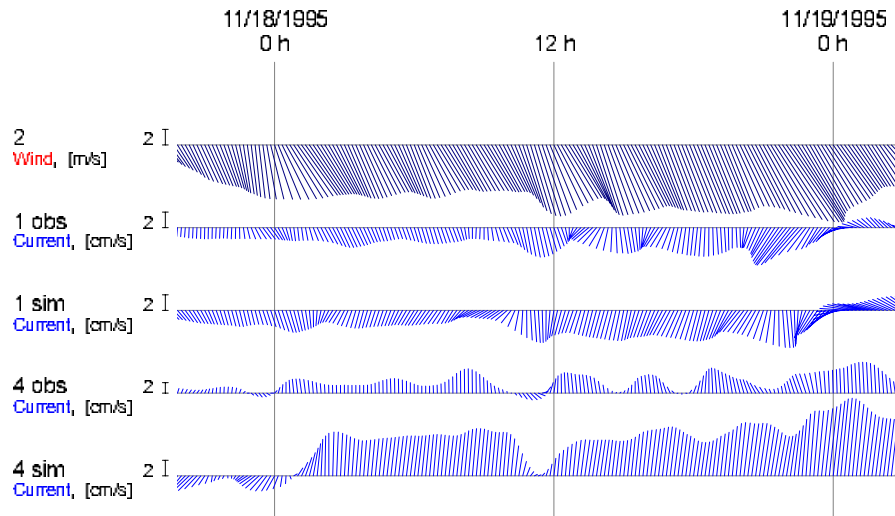
Fig. 10. Stick plot of observed wind (top row), observed and simulated currents (rows below) for Station 1 and 4 (see *Fig. 9*). The time series were smoothed by a 1-hour low-pass filter to facilitate comparison.
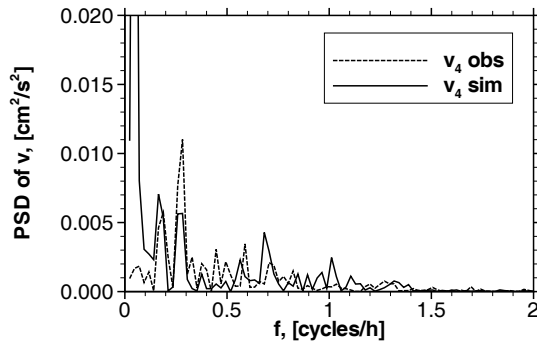
Fig. 11. Power spectral density function of the observed and simulated currents at Station 4, calculated after resampling to uniform 10-minute interval.

6. Steady-state Circulation in Lake Neusiedl

Currents in lakes are not as persistent as oceanic eddies because they are generated by inherently unsteady storms of finite duration. However, the long-term transport tendencies are related to the steady-state circulation induced by prevailing winds. The area of Lake Neusiedl is known for high wind potential, which is harvested by a 240 MW wind farm on the northern side of the lake. The prevailing wind direction is north-northwest (NNW), which is also the direction of highest average wind energy input.

The currents generated by a steady-state, prevailing wind forcing were simulated with the model. Wind forcing was assumed to vary with the fetch across the lake according to the changing surface roughness z_0. The abrupt change of z_0 at the boundary between the reed and the open lake gives rise to an internal boundary layer [17]. The roughness height over the open lake is estimated by the Charnock relation $z_0 = 0.0185\, w_*^2/g$, in which $w_* = (0.8 + 0.065\,|\mathbf{w}_{10}|)10^{-3}\mathbf{w}_{10}^2$; here $|\mathbf{w}_{10}|$ represents the local, fetch-dependent wind speed over the lake at 10 m height. Wind shear stress was computed according to the following parameters: wind speed at 10 m height over upwind terrain $|\mathbf{w}_{10}| = 10$ m/s; wind direction $\varphi = 300°$ (NNW); density of air $\rho_{air} = 1.225$ kg/m^3; roughness height of reed above the water surface $z_{0,\mathrm{reed}} = 0.2$ m. As to the remaining model parameters, they were set as for the previous unsteady simulation. The simulation ended at $t_{\mathrm{stop}} = 72$ h.

In constrast to the unsteady simulation where the target area was the Fertőrákos Bay, here a lakewide picture of the circulation patterns is sought. To this aim, the initial mesh was generated by specifying at least 800 m cell size over the lake, 400 m on the reed boundary and 100 m near impervious embankments and narrow straits (leftmost panel in *Fig. 12*). The mesh was adapted to the solution every 6 h starting at $t = 37$ h, with a refinement sensitivity $s_a = 0.2$ and coarsening parameter $a_{coa} = 0.1$. The total cell count was limited to $3\times$ the initial count (9120 cells), and the minimum cell size was set to 100 m in the open lake and 200 m in reed covered areas.

It can be seen from *Fig. 12* that the mesh density was increased nearly uniformly over the open lake. Additional refinement occurred primarily on the interface between the reed and the open lake. The error estimator thus recognized the sudden change in medium properties and depth through their effect on the velocity field. The refinement automatically results in a better approximation of the bathymetry and vegetation coverage. After three adaptation steps (see the middle panel), refinement has already reached its maximum level in the strait near Fertőrákos that carries the bulk of the discharge between the southern and northern basins (*Fig. 5*). The accurate estimation of the conveyance in that zone is crucial for the modelling of not only the local, but also lake-wide seiche and transport processes. Indeed, the mesh must be sufficiently refined to approximate faithfully the cross section of the strait with an integer number of cells.

The convergence history of the solution recorded at different points in the open lake (*Fig. 13*) demonstrates that the first adaptation step was requested
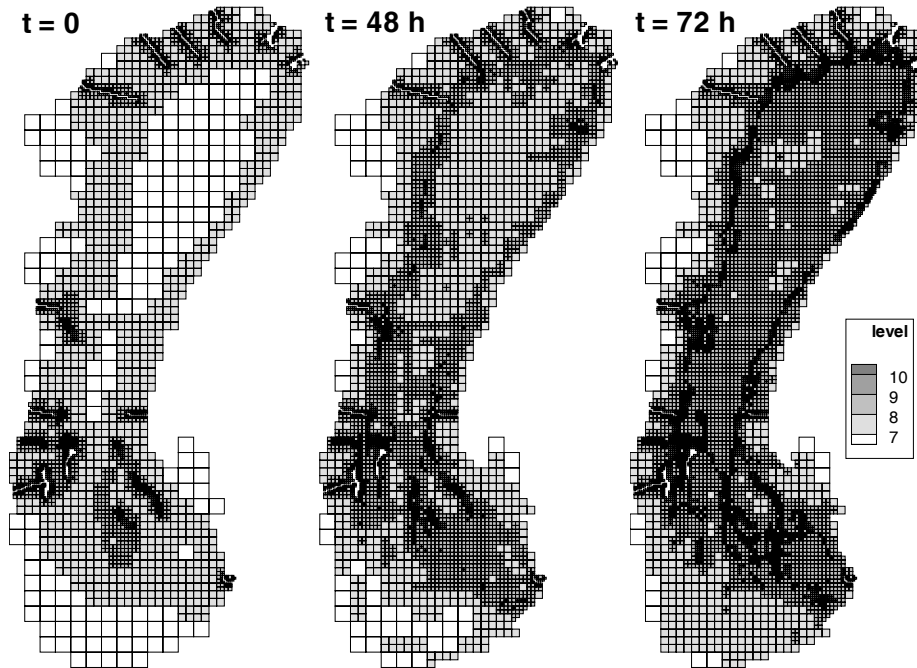
Fig. 12. Initial, intermediate and final stage of mesh adaptation.

(at $t = 37$ h) only after the steady state has been approached on the coarse initial mesh. A premature adaptation would have increased the cell count too early, unnecessarily slowing down the simulation. It can also be seen from the plots that the first few adaptation steps caused appreciable changes in the velocity, whereas later refinements were less effective. Introducing further adaptation steps is therefore not justified for this steady-state simulation, as the overhead would add to the computation time without notably improving the accuracy. This adaptation strategy in fact realises one prolongation step of a multigrid scheme. The transfer of the coarse solution towards the finer meshes is achieved in an adaptive way, refining only where the expected accuracy improvement justifies it. The adaptations caused a disturbance in the solution not only because the water surface had to be adjusted to the refined or coarsened bathymetry in order to conserve volume locally, but also due to the nonlinearity of the momentum equations. The disturbance was more pronounced for the velocity than for the surface elevation because the water surface varies more smoothly over the lake than the velocity field.

To see how refinement affects the numerical solution, the converged velocity field is shown in *Fig. 14* for three different adaptation step counts. The same rectangular area with dimensions 4.5×4.5 km, situated in the northwestern part of the lake is displayed in all panels. The top row shows the velocity vectors plotted
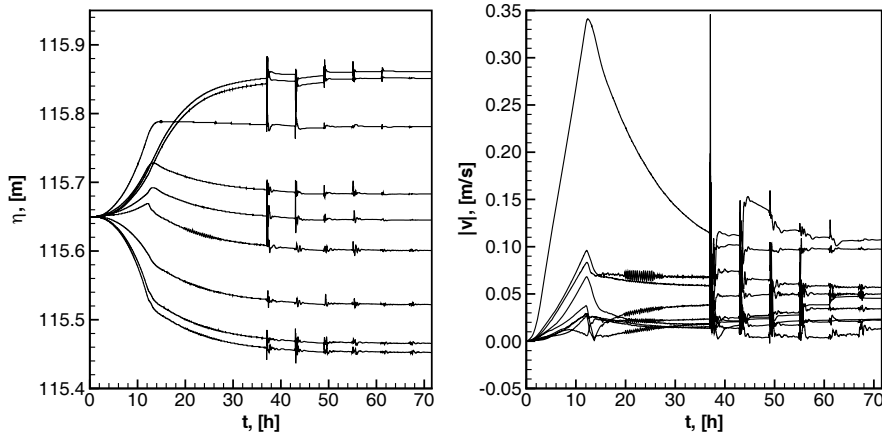
Fig. 13. Convergence history of water elevation (left) and velocity magnitude (right) at different points in the lake, in response to NNW wind.

in cell centres, the bottom row shows a linearly resampled field. The columns, from left to right, stand for the converged solution on the initial mesh (*0 ad.*), on a mesh adapted in two steps (at *t* = 37 and 43 h, displayed as *2 ad.*), and on the mesh in *Fig. 12* which was adapted at 6-hour intervals till the end of the simulation (*6 ad.*). It is apparent from a comparison of the uniformly resampled velocity fields in *Fig. 14* that the overall flow pattern obtained on the coarse mesh is not significantly modified by solution adaptation. However, the model is unable to resolve eddies smaller than the mesh size, such as the lower eddy near the reed boundary which develops fully only after the mesh has reached sufficient density there. This implies that the local accuracy of the modelled currents is sensitive to the mesh resolution in zones with highly convolute velocity field. The degree of convolutedness of the velocity field would then be quantified by the error estimator.

   Fig. 15 depicts the modelled circulations in the larger part of the lake. The left panel shows the velocity vectors resolved by the final mesh. In the right panel, the linearly resampled vector field and the currents measured at five stations during a steady NNW storm on May 3, 1992 are displayed. The measurements are smoothed with a 6-hour low-pass filter in order to separate the steady circulations from the oscillatory components, and magnified to five times the scale of the underlying simulated flow pattern for emphasis. The agreement of the numerical solution is reasonable. The numerical solution on the coarse mesh may accurately represent the exact solution averaged over the cells, but the level of detail on the initial mesh shown in *Fig. 14* may be insufficient for assessing model accuracy with pointwise field measurements. Of course, the error indicators evaluated on the final mesh can be used to estimate by how much the accuracy would have been improved with
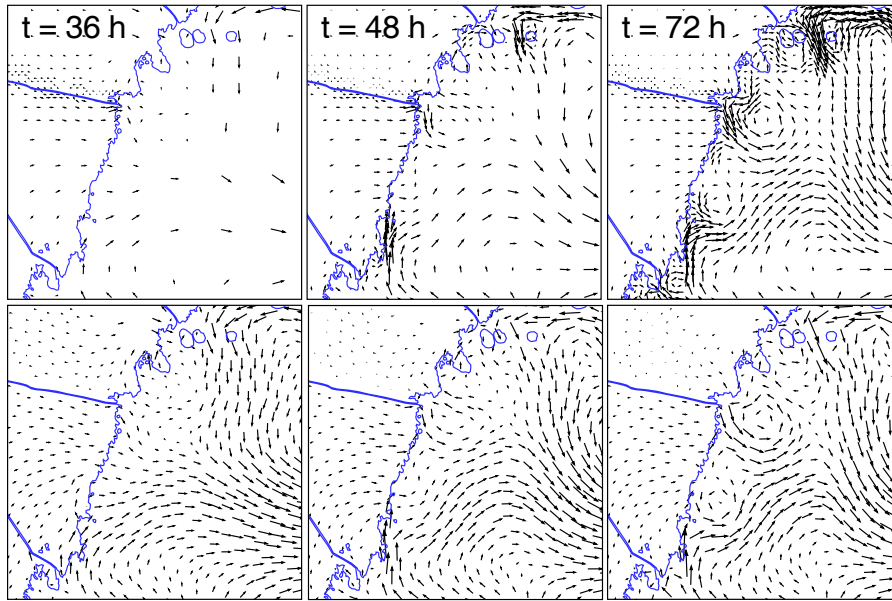
Fig. 14. Effect of mesh resolution on the modelling of the gyres. Top row: velocity vectors resolved by the mesh. Bottom row: vectors resampled with Poisson-disk distribution.

futher mesh refinement. This *a posteriori* error assessment is even applicable to solutions based on fixed, regular grids.

7. Conclusions

In this paper, we have presented a high-resolution Godunov-type finite-volume solver with solution-adaptive capability and applied it to simulate wind-driven circulation in the shallow, vegetated Lake Neusiedl. In addition to commonly used shallow water models, the physical description accounts for the wave-induced bed shear stress and the fetch dependency of wind shear stress. The HLLC Riemann solver coupled with the wetting-and-drying algorithm and automatic timestep control successfully overcame the numerical difficulties caused by the lateral movement of the shoreline.

The quadtree-based mesh was found robust and flexible for use in a natural lake with complex inner boundaries. The generation of the mesh is fully automatic and nonarbitrary (as opposed to the generation of triangular meshes), still the modeller has control over the distribution of the desired level of detail. When simulating
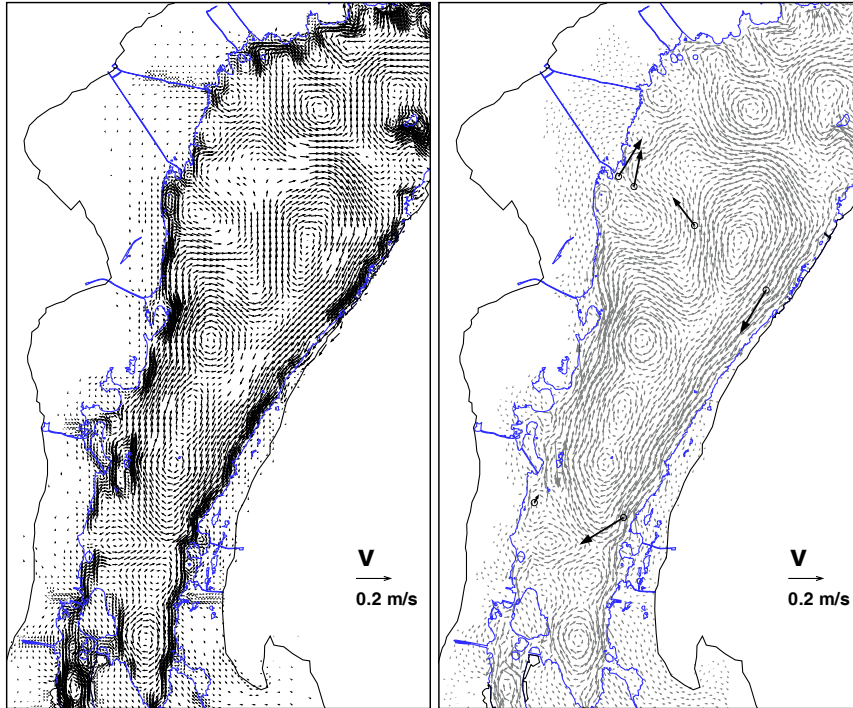
Fig. 15. Modelled steady state velocity field driven by NNW wind. Left: vectors in the resolution of the model. Right: vectors resampled linearly with Poisson disk distribution at ~200 m spacing. The large dark arrows show the 5× magnified, time-averaged local velocities observed during a sustained two-day NNW storm.

the unsteady lake response to wind forcing in Fertőrákos Bay, the whole lake was represented on a coarse mesh with adequate cell resolution to model the effect of the longest seiche modes on the Bay boundaries, while a higher mesh density was employed in the Bay itself to raise the level of detail locally.

The estimated solution error automatically controls the adjustment of the initial mesh in order to balance computational effort and accuracy. This way, solution-adaptation alleviates the need for the modeller's consideration of the numerical errors when manually prescribing mesh density based on the variability of topography and hydraulic resistance. As a precautionary measure, the initial mesh must be at least as fine locally as the smallest bed feature to be explicitly represented in the model, because the averaging in large cells may prevent the error estimator from discovering the subscale variability of the bed.

A different adaptation scheduling was used for the unsteady and the steady-

state simulation. In the unsteady case, the adaptation – refinement and coarsening – was performed regularly, in accordance with the time variability of the wind forcing. On the other hand, the simulation of the steady-state circulation was accelerated by letting the solution converge on the coarse initial grid, then performing successive refinement steps to reduce errors arising from unsufficient mesh resolution.

Future work will include the approximation of surface forces that takes into account the subgrid-scale geometry analytically to avoid excessive refinement in patchy vegetation. Moreover, the achievable accuracy improvement using a more elaborate formulation for vegetation resistance and bottom friction should be investigated.

8. Acknowledgement

References

[1] ADCROFT, A. – MARSHALL, D. How Slippery are Piecewise-constant Coastlines in Numerical Ocean Models? *Tellus A*, **50** (1998), pp. 95–108,.

[2] BORTHWICK, A. G. L. – CRUZ LEÓN, S. – JÓZSA, J., The Shallow Water Equations Solved on Adaptive Quadtree Grids. *International Journal for Numerical Methods in Fluids*, **37**, (2001), pp. 691–719.

[3] BRADFORD, S. F. – SANDERS, B. F., Finite-volume Model for Shallow-water Flooding on Arbitrary Topography. *Journal of Hydraulic Engineering*, 128:289–298, 2002.

[4] COIRIER, W. J., *An adaptively-refined, Cartesian, Cell-based Scheme for the Euler and Navier-Stokes Equations*. PhD thesis, NASA Lewis Research Center, Cleveland, OH, USA, October 1994.

[5] CROSSLEY, A. J. – WRIGHT, N. G. – WHITLOW, C. D., Local Time Stepping for Modelling Open Channel Flows. *Journal of Hydraulic Engineering*, **129/6** (2003), pp. 455–462.

[6] DE ZEEUW, D. L., *A Quadtree-based Adaptively-refined Cartesian-grid Algorithm for Solution of the Euler equations*. PhD thesis, University of Michigan, 1993.

[7] FRACCAROLLO, L.– TORO, E. F., Experimental and Numerical Assessment of the Shallow Water Model for Two-Dimensional Dam-Break Type Problems. *Journal of Hydraulic Research*, **33/6** (1995), pp. 843–864.

[8] GÁSPÁR, C. – JÓZSA, J. –SARKKULA, J., Shallow Lake Modelling Using Quadtree-Based Grids. In A. Peters et al., editor, *Proceedings of the Xth International Conference on Computational Methods in Water Resources*, pp. 1053–1060, Heidelberg, 1994. Kluwer Academic Publisher.

[9] GRANT, W. D. – MADSEN, O. S., Combined Wave and Current Interaction with a Rough Bottom. *Journal of Geophysical Research*, **84** (1979), pp. 1797–1808.

[10] HUBBARD M. E. – DODD, N., A 2D Numerical Model of Wave Run-up and Overtopping. *Coastal Engineering*, **47/1** (2002) pp. 1–26.

[11] JÓZSA, J. – SARKKULA, J. – KRÁMER, T., Wind Induced Flow in the Pelagic Zones of Lake Neusiedl. In H. Bergmann et al., editor, *CD-ROM Proceedings of the XXVIII IAHR Congress*, 1999.

[12] KLEB, W. L. – BATINA, J. T.– WILLIAMS, M. H., Temporal Adaptive Euler/Navier-Stokes Algorithm Involving Unstructured Dynamic Meshes. *AIAA Journal*, **30** (1992) pp. 1980–1985.

[13] POETER, E. P. –HILL, M. C., Documentation of UCODE, a Computer Code for Universal Inverse Modelling. Technical Report Water-Resources Investigations Report 98-4080, U.S. Geological Survey, 1998.

[14] ROGERS, B. – FUJIHARA, M. – BORTHWICK, A. G. L., Adaptive Q-tree Godunov-type scheme for Shallow Water Equations. *International Journal for Numerical Methods in Fluids*, **35** (2001), pp. 247–280.

[15] SHU, C. W. – OSHER, S., Efficient Implementation of Essentially Non-Oscillatory Shock-Capturing Schemes. *Journal of Computational Physics*, **77** (1988) pp. 439–471.

[16] SMAGORINSKY, J., General Circulation Experiments with Primitive Equations, I. The Basic Experiment. *Monthly Weather Review*, **91** (1963), pp. 99–164.

[17] TAYLOR, P. A. – LEE, R. J., Simple Guidelines for Estimating Wind Speed Variability due to Small-scale Topographic Features. *Climatological Bulletin*, **18** (1984) pp. 3–14.

[18] Y.-H. TSENG – J. H. FERZIGER. A Ghost-cell Immersed Boundary Method for Flow in Complex Geometry. *Journal of Computational Physics*, **192/2** (2003), pp. 593–623.

[19] U.S. Army Corps of Engineers, Coastal Engineering Research Center, US Government Printing Office, Washington, DC. *Shore Protection Manual*, fourth edition, 1984.

[20] ZHAO,D. H.– SHEN, H. W.– TABIOS III, G. Q. – LAI,J. S. – TAN, W. Y. Finite-volume Two-dimensional Unsteady-flow Model for River Basins. *Journal of Hydraulic Engineering*, **120** (1994), pp. 863–883.